Cylindrical Domains of Block Copolymers Developed via Ordering under Moving Temperature Gradient: Real-Space Analysis

Kazuki Mita,[†,||] Mikihito Takenaka,[†,‡] Hirokazu Hasegawa,[†] and Takeji Hashimoto*[,†,§]

Department of Polymer Chemistry, Graduate School of Engineering, Kyoto University, Katsura, Nishikyo-ku, Kyoto 615-8510, Japan; Structural Materials Science Laboratory, SPring-8 Center, RIKEN Harima Institute Research, Hyogo 679-5148, Japan; and Advanced Science Reserch Center (ASRC), Japan Atomic Energy Agency (JAEA), Tokai-mura, Ibaraki-Pref. 319-1195, Japan

Received August 1, 2008; Revised Manuscript Received September 8, 2008

ABSTRACT: We applied the zone heating method to cylinder-forming diblock copolymers (bcp) for controlling the orientation of the hexagonally packed cylindrical microdomain structures (hex-cyl) and reported the results of the structure analysis by small-angle X-ray scattering (SAXS) in our previous paper [Mita et al. *Macromolecules* **2007**, *40*, 5923]. In this report, we present the results of the real-space analysis of the zone-heated bcp by using polarized optical microscopy and transmission electron microscopy. The real-space analysis elucidated that the zone heating creates the columnar-shaped grains extending along the temperature gradient (∇T) direction: within a given grain the cylinder axes are aligned perpendicular to ∇T axis with a fixed rotational angle ϕ around ∇T axis: the angle ϕ varies statistically randomly over many grains. These results firmly verified the columnar grain model proposed by the previous Fourier-space analysis. Furthermore, the real-space analysis elucidated the average lateral size and shapes of the grains, the commensuration of the hex-cyl at the grain boundaries, and the fact that this commensuration was achieved by the distortion of the domain spacing of the hex-cyl near the grain boundaries from its equilibrium value.

1. Introduction

In our previous papers,[1−3] we have reported how a zone-heating method can control the macroscopic orientation of a hexagonally packed cylindrical microdomain structure (hex-cyl) on the basis of Fourier-space analysis with the small-angle X-ray scattering (SAXS) method. With this method, we imposed a moving temperature gradient (∇T) on polystyrene-*block*-polyisoprene (SI) diblock copolymer (bcp) during its ordering process from the disordered melt to the hex-cyl. The method was found to create the special texture of the so-called "columnar grain" of the hex-cyl, as illustrated in Figure 1. Most of the hex-cyl (∼98 wt %) have the following orientation as shown in Figure 1a (major orientation); the cylinder axes and the (100) planes of the hex-cyl orient perpendicular to the ∇T axis (defined as the Oz axis). Providing that the direction of the cylinder axes in each grain is designated by the rotational angle ϕ around the ∇T axis, the value ϕ has a fixed value in each grain but varies among different grains, giving rise to macroscopically random rotation. Besides the major orientation of the hex-cyl mentioned above, the minor orientation with the (110) planes perpendicular to the ∇T axis is also allowed, as shown in Figure 1c.

The SAXS analyses elucidated that the texture consists of volume-filling columnar grains of the hex-cyl with the column axes extending parallel to the ∇T axis. The columnar grains result from the "sequential ordering" induced by the glass surface[4] and the moving ∇T which enhances the longitudinal growth of the grains along the ∇T direction relative to the lateral growth normal to it. The lateral growth of the grain is limited by impingements with other laterally growing grains, while the longitudinal growth is essentially unlimited as long as the growing front faces to disordered melts, which is likely to be assured by the sequential ordering. This extrinsic effect related to the lateral impingements is expected to cause a large aspect ratio of the columnar grains and unique "columnar grain boundaries" of hex-cyl.

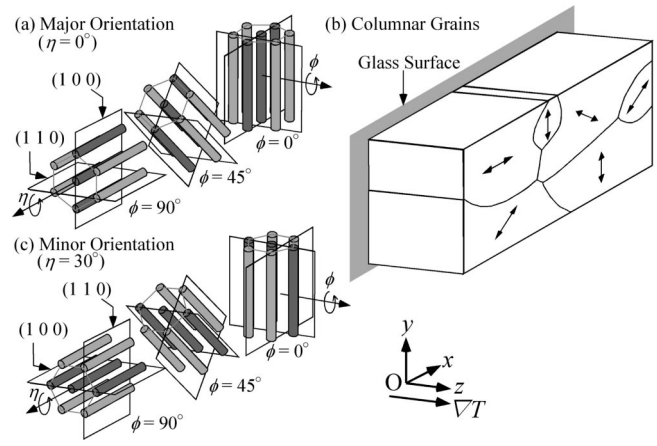

Figure 1. Illustrations of the model for the special texture of the hex-cyl developed by the zone heating process. In the grains having the major orientation (a), (100) planes of the hex-cyl are perpendicular to the z axis (∇T axis), but the cylinder axes are randomly rotated around the z axis within the planes parallel to the xy plane with the rotation angle ϕ. The grains grow along the z axis to have a "columnar" shape with keeping the fixed ϕ and η values within the given grains (b). The arrows marked in the grains represent the orientation of the cylinder axes within the grains. In minor orientation (c), (110) planes are perpendicular to the z axis.

In the previous SAXS studies,[1,2] we could not estimate the lateral size of the grains. Moreover, we could not get information on the shapes of the grains and on the grain boundary structure (GBS). Here, we shall present a full real-space analysis of the zone-heated specimen in order to further enrich information concerning these unsolved problems.

We would like to emphasize here that the columnar grains will provide an excellent and interesting model system to study the GBS of hex-cyl in general. We anticipate that the GBS

* To whom correspondence should be addressed.
† Kyoto University.
‡ RIKEN Harima Institute Research.
§ Japan Atomic Energy Agency.
|| Present address: R&D Center, Mitsui Chemicals, Inc., 580-32 Nagaura, Sodegaura, Chiba 299-0265, Japan.

10.1021/ma801750c CCC: $40.75
Published on Web 10/29/2008

Table 1. Characteristics of the Sample Used in This Paper[a]

code	M_n	M_w/M_n	f_{PI}	T_{ODT}
YM-1	2.3×10^4	1.04	0.31	147 °C

[a] M_n: number-average molecular weight estimated by GPC. M_w/M_n: polydispersity index where M_w is weight-average molecular weight measured by GPC. f_{PI}: volume fraction of polyisoprene estimated by using M_n of each block and assuming densities of PS and PI in the system to be equal to those of corresponding homopolymers.[18,19] T_{ODT}: order−disorder transition temperature evaluated by SAXS.

elucidated for the columnar grain is important also for general studies of the GBS of hex-cyl in bcps in the light of almost no information available for the GBS of hex-cyl except a few[5,6] to the best of our knowledge. Generally real-space information on GBS in bcps is fairly rare compared to that in liquid crystal systems (see for example ref 7). Moreover, most of the rare information is focused on the GBS of lamella.[8−12] In view of these historical backgrounds, we believe it is important for us to try our best effort to get, with elaborate and careful analyses, all the requisite real-space information on the GBS of the columnar grain. In this paper we aim to report the real-space information obtained along this line. We hope the report will give some impacts on physics of the GBS of hex-cyl of bcps in general.

2. Experimental Method

2.1. Sample. The characteristics of SI bcp (coded as YM-1) used in this study are summarized in Table 1. The sample of YM-1 was mixed with antioxidant (Irganox1010) and cast from a homogeneous solution in toluene with a total polymer concentration of 10 wt %. The film specimens thus obtained was annealed in vacuum (for 8 h at 120 °C) before applying the zone heating. The film specimens had a hex-cyl of polyisoprene (PI) block chains in the matrix of polystyrene (PS) block chains.[2] The Bragg spacing corresponding to the spacing of (100) plane, D_{100}, and order−disorder transition (ODT) temperature, T_{ODT}, as measured by SAXS were 18 nm and 147 °C, respectively.[2]

2.2. Zone Heating. We used a "zone heating apparatus" described elsewhere,[1] in order to impose moving ∇T on a specimen. In this experiment, we used a sharp nominal temperature gradient of $|\nabla T|_{nom} = 62$ °C/mm between $T_2 = 190$ °C and $T_1 = 5$ °C. The temperature gradient crosses T_{ODT} of YM-1. As shown in Figure 2a, we set the Cartesian coordinate Oxyz fixed to the specimen with its origin being set at the center of the glass surface, which contacted the specimen with Oxy plane. We used polystyrene (PS)-grafted glass surface, the preparation method of which was described elsewhere.[13,14] The ∇T applied to the specimen moved along the Oz axis. We used the smallest moving rate of ∇T of 25 nm/s ($1.4D_{100}$/s), which gave rise to the highest selectivity of the major orientation among our experiments using YM-1 or other dibcp.[2] The effective temperature gradient $|\nabla T|_{eff}$ was determined by measuring temperature at a given point in the specimen with a thermocouple embedded in it as a function of time for each condition, as detailed elsewhere.[1] Thus, evaluated $|\nabla T|_{eff}$ was 22 °C/mm (4.0×10^{-4} °C/D_{100}) and much smaller than $|\nabla T|_{nom}$, probably due to the conduction of heat within the specimen.

2.3. Polarized Optical Microscopy. Polarized optical microscopy (POM) was conducted in order to investigate a spatial distribution of form birefringence, which reflects a spatial organization of the grains of hex-cyl in the zone-heated specimen, and to clarify the shapes and the orientation of the grains. The specimen for POM observations was cut out from the as-prepared zone-heated specimen, which was spontaneously solidified in the zone-heating process, into a rectangular parallelepiped as shown in Figure 2a: The specimen extends along Ox, Oy, and Oz directions with $0.5 \le x$/mm ≤ 2.0, $-1.0 \le y$/mm ≤ 1.0, and $0 \le z$/mm ≤ 2.0. Here, the Cartesian coordinate Oxyz was fixed to the specimen with its origin right at the center of the glass surface. Therefore, the thickness of the specimen along the Ox, Oy, and Oz axis is 1.5, 2.0, and 2.0 mm, respectively.

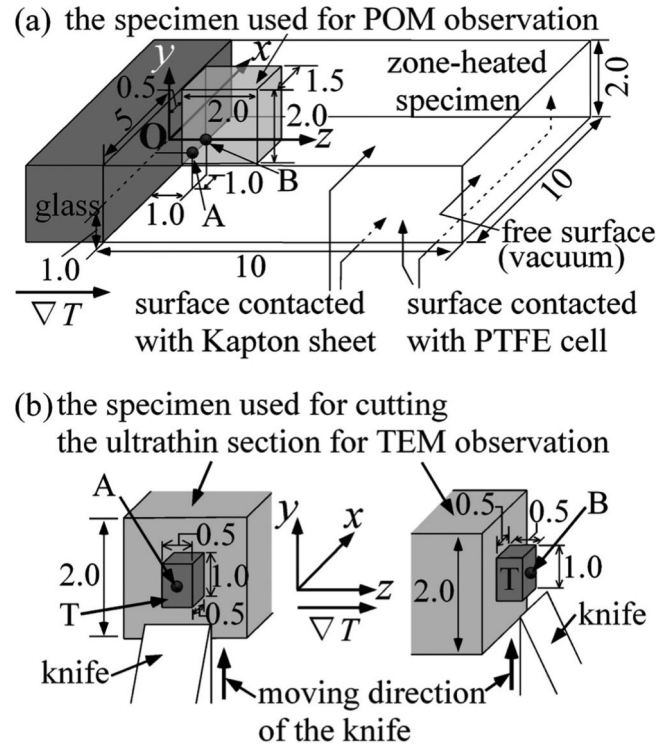

Figure 2. (a) Schematic diagram showing the geometric relationship between the specimen and the Cartesian coordinate. During the zone heating process, the film specimen was placed inside the cell made out of polytetrafluoroethylene (PTFE) with a glass surface on one end of the specimen surface. Thin Kapton sheets were placed on both surfaces of the specimen parallel to the xz plane. The origin of the Cartesian coordinate was set to be the center of the glass surface in contact with the specimen. The specimen for POM observation was cut from the zone-heated, solidified specimen as indicated by the light gray rectangular parallelepiped, which extends along Ox, Oy, and Oz directions by $0.5 \le x$/mm ≤ 2.0, $-1.0 \le y$/mm ≤ 1.0, and $0 \le z$/mm ≤ 2.0, respectively. The ultrathin sections for TEM observations were sliced perpendicular to x axis and z axis including point A (x, y, z) = (-1.0, 0, 1.0) and point B (x, y, z) = (0, 0, 1.0), respectively. (b) Magnified schematic illustration showing preparation of the ultrathin section including point A or point B. The specimen including point A or B was microtomed into the ultrathin section by a glass knife set parallel to the yz or xy plane, respectively. The knife moved along the y axis for both cases. In both (a) and (b), the numbers in the figure indicate the lengths in unit of millimeters.

The specimen thus prepared was observed at room temperature from the Ox and Oz directions, which are perpendicular and parallel to the ∇T direction, respectively, with a polarized optical microscope (OPTIPHOTO-POL, Nikon Corp., Tokyo, Japan) equipped with a charge coupled device (CCD) camera (XC-999, Sony Corp., Tokyo, Japan) as a detector. The specimen was immersed in silicone oil (KF-54, Shin-Etsu Chem. Corp., Tokyo, Japan) to reduce the total reflection due to the cracks developed in the specimen during the cutting process. The observations were carried out for the specimen under crossed-nicols with a retardation plate having a retardation Γ_p ($\Gamma_p = 147$ nm) or without the plate ($\Gamma_p = 0$). In order to evaluate the retardations of specimen in each POM image, we used an interference color chart, which enable us to translate observed interference colors to corresponding retardation values.[15]

2.4. Transmission Electron Microscopy. Transmission electron microscopy (TEM) was conducted by using a JEOL JEM-2000FXZ transmission electron microscope operated at 120 kV in order to confirm the orientation of the hex-cyl clarified by SAXS[1,2] and to get information about the shape of the grains. We prepared two kinds of ultrathin sections from the zone-heated specimen, as shown in Figure 2b. One was sliced perpendicularly to the Ox axis in order

to observe the image in the *yz* plane, which is parallel to the ∇T direction, and the other was sliced perpendicularly to the O*z* axis in order to observe the image in the *xy* plane, which is perpendicular to the ∇T direction. The former and the latter sections were sliced from the positions at A (x, y, z) = (−1.0, 0, 1.0) and B (x, y, z) = (0, 0, 1.0), as designated in Figure 2a,b.

In order to prepare those ultrathin sections as described above, we first cut each bit (a small rectangular parallelepiped) of the specimen including point A or B from the solidified specimens. The each bit retained the surfaces in contact with the polyimide (Kapton) sheets as well as the surface in contact with the glass surface, both of which are used as the reference planes parallel to the *xz* plane and *xy* plane, respectively. We further cut each bit (the light gray object) to prepare a trimmed smaller rectangular parallelepiped (the dark gray object designated by T) which has surfaces parallel to the *xy*, *yz*, and *zx* planes, as shown in Figure 2b. Then the trimmed portion of each bit was microtomed as shown in Figure 2b into ultrathin sections of ca. 50 nm thickness at −90 °C with a Reichert-Nissei ULTRACUT N ultramicrotome together with a cryogenic unit FC 4E and a glass knife set parallel to the *yz* or *xy* plane, respectively. The glass knife moved along the O*y* axis for both cases. The direction of the O*y* axis in the TEM images was identified by the knife marks observed on the ultrathin sections, as will be mentioned later in section 3. In this way we can unequivocally identified the Cartesian coordinate for the observed TEM images. The ultrathin sections were picked up on 400 mesh copper grids and stained by the vapor of 2% O_sO_4(aq) for 1 h at room temperature. Therefore, PS and PI domains are observed bright and dark in TEM images, respectively.

3. Results

3.1. POM Observations. *a. POM Observations along the Ox Direction with Γ_p = 0 (without a Retardation Plate).* The POM images of the zone-heated specimen at $\mu_x = 45°$ and $\mu_x = 0°$ are shown in parts a and b of Figure 3, respectively, where μ_x is the angle between O*z* axis and the polarization direction of polarizer P. Here, we note that dark curved lines observed in the POM images in Figure 3 are cracks in the specimens and will not be discussed further. The POM image becomes brightest at $\mu_x = 45°$ (Figure 3a) and darkest at $\mu_x = 0°$ (Figure 3b). This result is consistent with the model illustrated in Figure 1a,c, indicating that the cylindrical microdomains causing the form birefringence are oriented with their axis perpendicular to the O*z* direction. Figure 3a exhibits plural interference colors related to the rotational angle (ϕ) of cylinder axis around O*z* axis in the *xy* plane and the regions having the same color all extend along the O*z* axis. This result is consistent with the "columnar" grains as illustrated in Figure 1b. We will discuss the interference colors in conjunction with the results of POM observations with the retardation plate of $\Gamma_p = 147$ nm in section 4.1.

b. POM Observations along the Oz Direction with Γ_p = 0. The POM images at $\mu_z = 0°$ and $\mu_z = 45°$ are shown in parts c and d of Figure 3, respectively, where μ_z is the angle between O*y* axis and the polarization direction of polarizer P. According to the previous SAXS results,[1] the cylinder axes are oriented parallel to the *xy* plane. Therefore, in order to investigate the regions or grains within which the hex-cyl has a uniform orientation, we observed the same area of the specimen under crossed-nicol by changing μ_z stepwisely by 5°. Consequently, we found that the specimen consists of many regions exhibiting different appearances for different μ_z. Each region becomes brightest when the cylinder axes orient in the diagonal condition with respect to the cross-polarizers or at a specific μ_z.

As their representatives, we chose the largest regions that become brightest at $\mu_z = 0°$ or 45° and designated them by numbers 1−4 as shown in Figure 3c,d. The region designated by 1 is dark at $\mu_z = 0°$ but bright at $\mu_z = 45°$. On the other hand, regions 2−4 become bright at $\mu_z = 0°$ but dark at $\mu_z = 45°$. These observation results indicate that the birefringence or the direction of cylinder axis is kept constant along the thickness direction (the O*z* direction) within these regions, implying that each region may consist of only one grain. Furthermore, the rotational angle ϕ of the cylinder axis in region 1 is different from that in regions 2−4. This is consistent with the "columnar" grains as illustrated in Figure 1b.

From the POM observation it was also shown that the cross sections of the columnar grains have more or less an elliptical shape on statistical average and spread over the area of 60−130 μm in a given direction in the plane parallel to *xy* plane. Although such information cannot be obtained by the TEM observation to be detailed in section 3.2, the TEM images observed from the O*z* direction also imply the existence of huge grains having an elliptical cross-sectional shape in *xy* plane on statistical average. On the other hand, the small grains, which cannot be resolved by the POM observations, exist between the huge grains.

c. POM Observations along the Ox Direction with Γ_p = 147 nm (with a Retardation Plate). Figure 3e shows the POM image under the crossed-nicols at $\mu_x = 45°$ with the insertion of the retardation plate R of $\Gamma_p = 147$ nm as shown in the figure. Plural interference colors are observed in Figure 3e. The solid lines drawn in Figure 3f correspond to the boundaries of the individual colored domains in Figure 3e. A total of 17 regions as designated by the numbers in Figure 3f can be distinguished by the colors, and each region was found to extend along the O*z* axis. This striped pattern is consistent with the columnar grains. The difference in the interference color of each region is due to the difference in the rotational angle ϕ of the cylinder axis around the O*z* axis as will be detailed in section 4. This is consistent with the columnar model in Figure 1. In all the regions from 1 to 17, the interference colors with $\Gamma_p = 0$ (Figure 3a), which can be classified into five different color levels as shown in Table 2 and represented by the regions 5, 6, 8, 9, and 11 in Figure 3a, are changed to the colors indicating larger retardations than those with $\Gamma_p = 0$ by the insertion of retardation plate of $\Gamma_p = 147$ nm (Figure 3e). This result indicates that the slow direction of the plate having the large refractive index n_L is matched with that of the form birefringence of the hex-cyl, so that two retardations due to hex-cyl and the plate add up, giving rise to a larger net retardation. Therefore, in all the regions, the cylinder axis orients perpendicular to O*z* axis, consistent with the models in Figure 1a,c.

d. POM Observations along the Oz Direction with Γ_p = 147 nm. Figure 3g shows the POM image under the crossed-nicols at $\mu_z = 0°$ with $\Gamma_p = 147$ nm. The inset of Figure 3g shows the POM image of region 1 under the conditions of $\mu_z = 45°$ and the slow direction of the plate R oriented along the O*y* axis. The results of the POM image analysis for regions 1−4 are indicated by the drawing with the refractive index ellipsoids for the form birefringence of each hex-cyl grain, as shown in Figure 3h. Here, the slow and fast directions of the form birefringence of the hex-cyl are parallel and perpendicular to the cylinder axes, respectively.

The retardation of region 1 determined by the interference color with $\Gamma_p = 147$ nm (inset of Figure 3g) is smaller than that at $\Gamma_p = 0$ (Figure 3d), indicating that the slow direction of the plate at $\mu_z = 45°$ is perpendicular to the slow direction of the form birefringence of the hex-cyl in region 1, so that Γ_p is compensated by the retardation of the sample. Therefore, ϕ, defined in Figure 1, is ∼90° or the cylinder axis is approximately parallel to the O*x* axis in region 1, as shown in the inset to Figure 3h. Here, we note that the values of ϕ determined by POM observations involve an error of ±5° due to the error in determination of the diagonal direction as mentioned above.

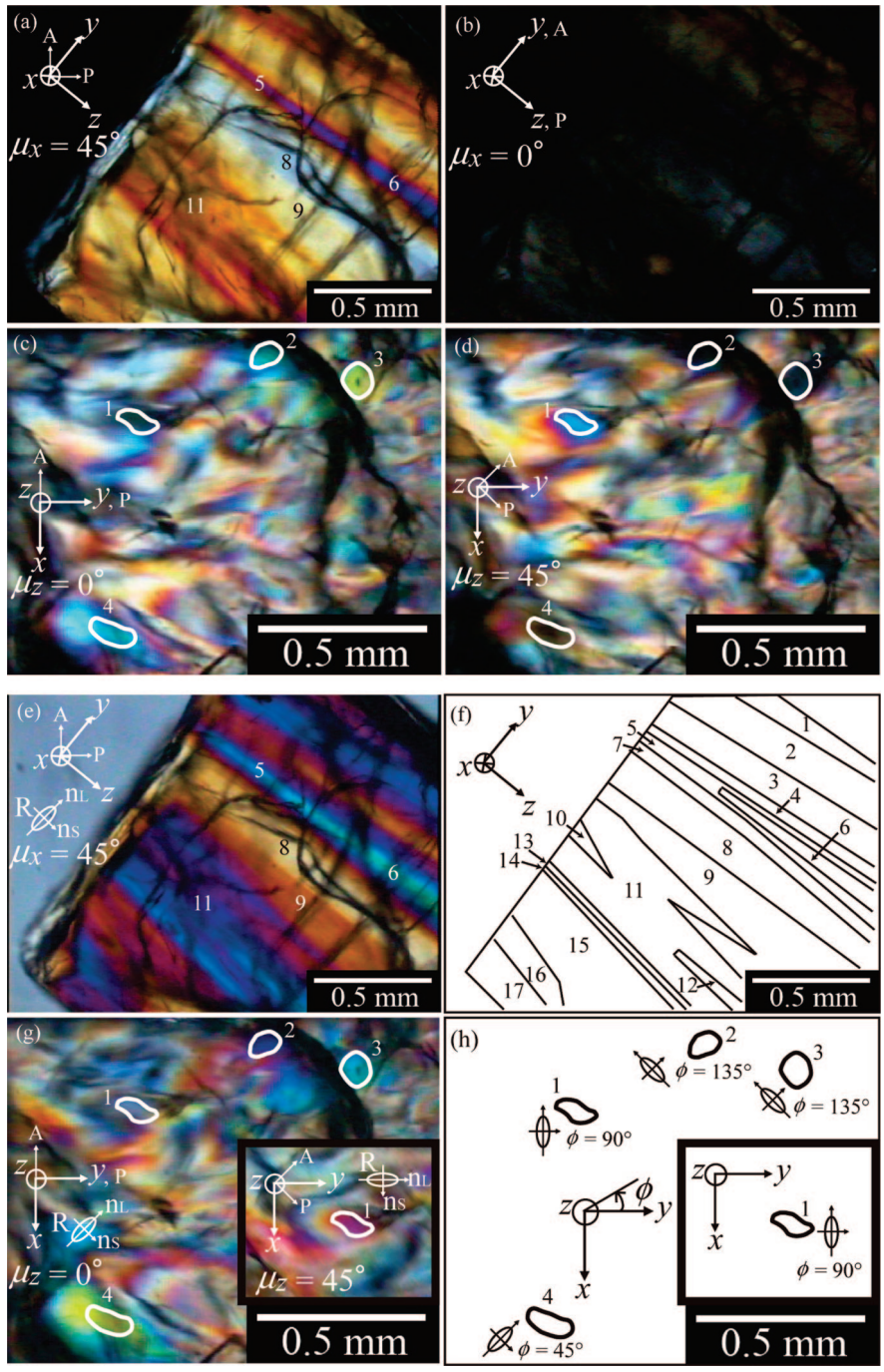

Figure 3. POM images of the specimen cut out from the zone-heated SI bcp films observed under the crossed-nicols: (a), (b), and (e) were observed along the O*x* direction, while (c), (d), and (g) were observed along the O*z* direction with the indication of the coordinate O*xyz* and the directions of the polarizer (P), analyzer (A), and the retardation plate R having the retardation 147 nm, if applicable. (a) $\mu_x = 45°$ and $\Gamma_p = 0$, (b) $\mu_x = 0°$ and $\Gamma_p = 0$, (c) $\mu_z = 0°$ and $\Gamma_p = 0$, (d) $\mu_z = 45°$ and $\Gamma_p = 0$, (e) $\mu_x = 45°$ and $\Gamma_p = 147$ nm, (g) $\mu_z = 0°$ and $\Gamma_p = 147$ nm, and inset of (g) $\mu_z = 45°$ and $\Gamma_p = 147$ nm. (f) shows schematic illustrations of the grains which were elucidated with the POM images (a), (b), and (e), and (h) shows the grains clarified with the POM images (c), (d), and (g).

Table 2. Results of Evaluations and Analyses of the Interference Colors

color level	region no.	color	$\Delta n_{f,x} \times 10^4$	$\langle \cos^2 \phi \rangle$
1	6	bluish violet	4.0	0.61
2	5, 12, 13	red purple	3.3	0.51
3	2, 4, 7, 11, 14, 16	brown yellow	2.7	0.40
4	1, 3, 9, 10, 15, 17	light yellow	2.0	0.30
5	8	light gray	1.3	0.20

In regions 2 and 3, the retardation determined by the interference colors with $\Gamma_p = 147$ nm (Figure 3g) is smaller than those with $\Gamma_p = 0$ (Figure 3c), indicating the slow direction of the plate at $\mu_z = 0°$ is approximately perpendicular to the slow direction of the form birefringence of the hex-cyl, so that these two retardations are canceled out. Therefore, ϕ is 135° in regions 2 and 3 as shown in Figure 3h. In region 4, the retardation determined by the interference colors with $\Gamma_p = 147$ nm (Figure 3g) is larger than those with $\Gamma_p = 0$ (Figure 3c), indicating that the slow direction of the plate at $\mu_z = 0°$ is parallel to that of the form birefringence of the hex-cyl, so that the two retardations add up, giving rise to a larger net retardation; hence $\phi = 45°$ in region 4 as shown in Figure 3h. Here, we picked up the grains with particular values of ϕ, but ϕ of the other grains can take any value. These results are consistent with the models in Figure 1.

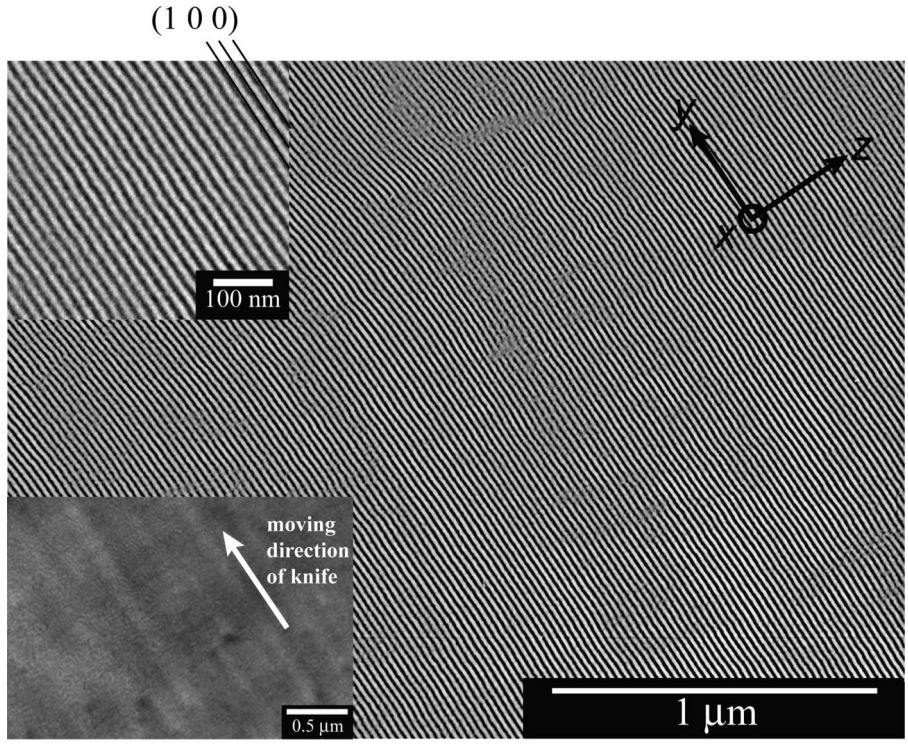

Figure 4. Typical TEM image obtained for an ultrathin section of the zone-heated SI bcp cut parallel to the *yz* plane and observed from the O*x* direction. The top-left inset shows a magnified image, where the striped pattern has the spacing corresponding to the (100) lattice spacing of the hex-cyl. The bottom-left inset is a lower magnification image of the same specimen exhibiting the knife marks (dark and bright bands) along the moving direction of the knife indicated by a white arrow, from which the *y* axis was assigned.

3.2. TEM Observations. *a. TEM Observations along the Ox Direction.* The TEM image of the zone-heated specimen observed from the O*x* direction exhibits the morphology projected on the *yz* plane, as shown in Figure 4. The inset in the top left shows a magnified image. The inset in the bottom left is the image with a low magnification, where dark and bright stripes of the knife marks can be observed along the white arrow. As already mentioned in section 2.4, the knife was moved along the O*y* axis, and the white arrow thus indicates the direction of the O*y* axis. We determined the O*y* axis for the other TEM images also from the knife marks.

In Figure 4, the alternating dark (PI) and bright (PS) stripes are observed. Each dark stripe corresponds to the projection of the PI cylinders in the (100) lattice planes onto the *yz* plane. The projections of the cylinders contained in the ultrathin section are superimposed along the O*x* direction, so that the more highly the PI cylinders are aligned on the planes, the larger the contrast difference between the two stripes become. The stripe pattern is uniform in the entire area of the figure and even extends over several 10 μm along the O*z* axis, suggesting that the zone heating method can produce the huge grains of the hex-cyl with the size of several 10 μm along the O*z* axis. The hex-cyl in this grain represents the major orientation with $\phi \sim 0°$, as shown in Figure 1a, because the stripes or the cylinder axes are oriented parallel to the O*y* direction, and their periodicity (17.8 nm) agrees with the spacing of (100) plane determined by the SAXS experiment (18 nm).[2]

In another ultrathin section cut parallel to the *yz* plane, a different type of TEM image was also observed, as shown in Figure 5. The inset in the top left shows a magnified image. A well-ordered hexagonal lattice observed in the entire area suggests that the PI cylinders are aligned with their axes perpendicular to the *yz* plane or the surface of the ultrathin section. In this image, (100) plane is perpendicular to the O*z* axis, and its spacing (18.4 nm) calculated from the hexagonal lattice agrees with that determined by the SAXS experiment.[2] These characteristics are consistent with the major orientation with $\phi \sim 90°$ shown in Figure 1a. Although the two images in Figures 4 and 5 are very different, the cylinder axes lie parallel to the *xy* plane in both cases.

Because of the extremely large grain sizes (60−130 μm) in the *xy* plane as observed for the columnar grains by POM in section 3.1, it is necessary to use much lower magnification than that employed in Figures 4 and 5 for TEM observation of the grain shapes. However, high-magnification images are necessary to resolve the microdomain structures and to distinguish the grain boundaries. Thus, it is extremely difficult to resolve simultaneously the microdomain and grain structures. Therefore, just to get evidence to prove the columnar grains extended along the O*z* direction by TEM observation, we chose a much smaller grain than those shown in Figures 4 and 5 and obtained a series of TEM images with a high magnification by shifting consecutively the view area. The extent of the shift must not exceed the limit so that every neighboring pair of the images shares a sufficiently large overlapping area and can be combined to form a single TEM image with a common O*xyz* coordinate to visualize the shape of the grain.

The image thus composed is shown in Figure S1 of Supporting Information 1, and some parts of the composed image and its schematic illustration are shown in parts b and a of Figure 6, respectively. An artificial stripe pattern having the spacing of 14 nm, as shown by the pattern A on both left and right edges of Figure 6b, was overlaid on the TEM images in Figure 6b in order to generate the Moiré fringes, through which the grain boundaries can be highlighted. The images b-1, b-2, and b-3 in Figure 6b were cut out from parts 1, 2, and 3 of the composed image, as illustrated in Figure 6a, respectively. The image b-1 was enlarged and shown without the artificial stripe pattern in Figure 6c.

In Figure 6a, dashed lines indicate grain boundaries G_1 and G_2 observed in the "patch work" described above. The middle narrow grain between two wider grains has a width of ca. 0.5

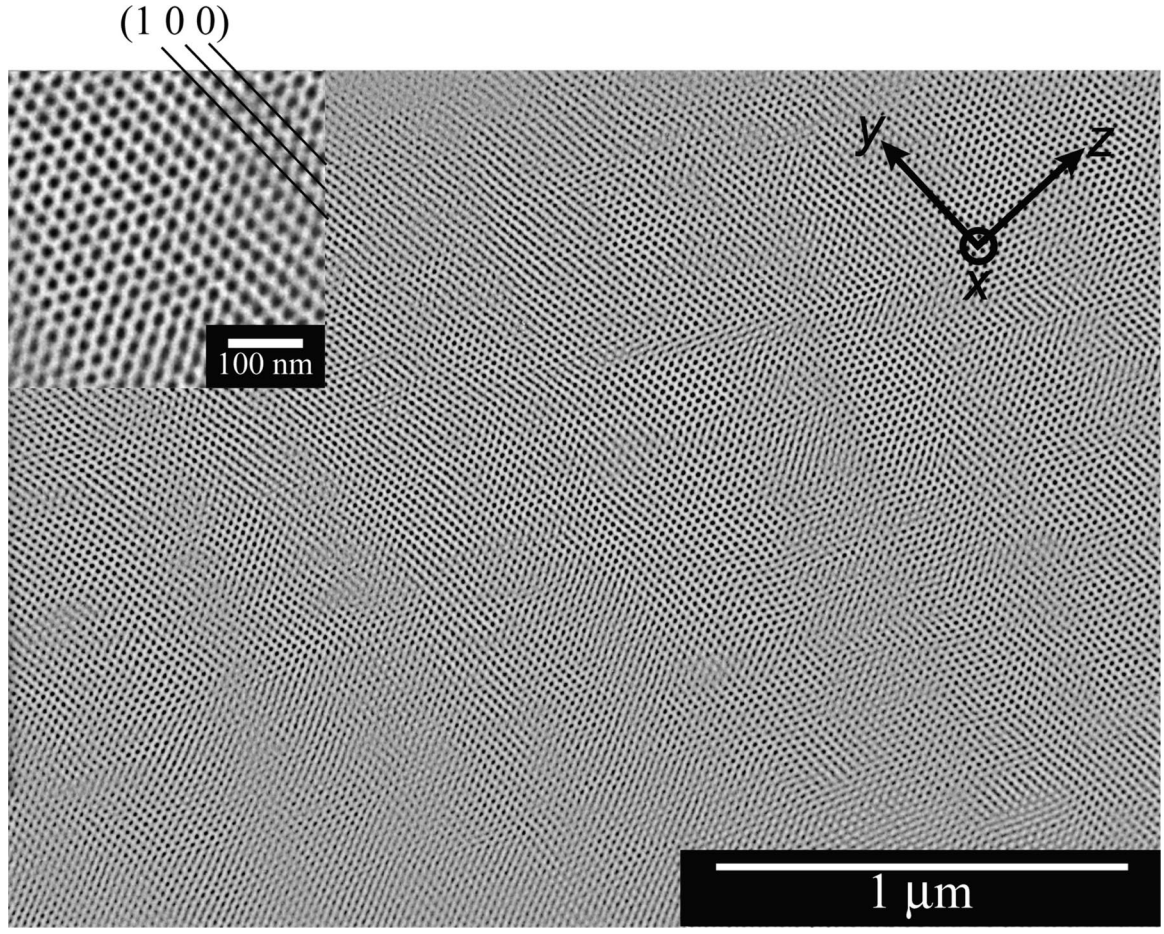

Figure 5. Typical TEM image obtained for another ultrathin section of the zone-heated SI bcp cut parallel to the *yz* plane and observed from the O*x* direction. The top-left inset shows a magnified image, where the hexagonal dot pattern has the spacing corresponding to the (100) lattice spacing of the hex-cyl. The O*xyz* coordinate was assessed in the same way as in Figure 4.

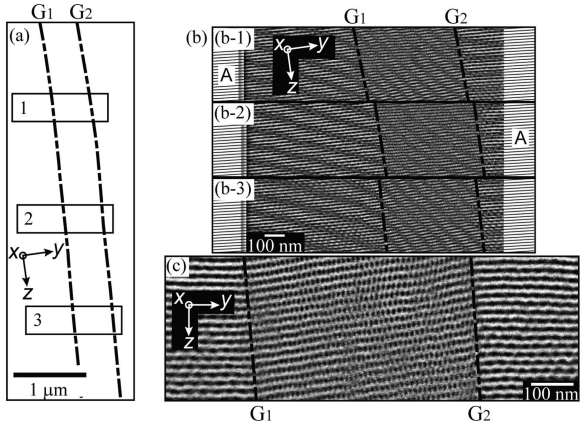

Figure 6. (a) Schematic illustration of the area of the ultrathin section of the zone-heated SI bcp cut parallel to the *yz* plane and observed by TEM from the O*x* direction. Dashed lines G_1 and G_2 indicate the grain boundaries, suggesting the grain growth along the *z* axis or ∇T direction. (b) Parts b-1 to b-3 correspond to the TEM images obtained from area 1 to 3 shown in part a. The artificial stripe pattern A was overlaid on the TEM images to create Moiré fringes, which make the grain boundaries conspicuous. (c) The enlarged image of part b-1 without the overlay of the artificial stripe. The three grains have the major orientation.

μm along the O*y* direction but spreads 5 μm at least along the O*z* direction. This result indicates that the middle narrow grain at least grew along the O*z* direction and became "columnar", as illustrated in Figure 1b. Figure 6b provides a piece of evidence for the existence of the three grains, all of which are continuous and extended along the O*z* direction as schematically indicated by Figure 6a, because the Moiré fringe in each grain remains unchanged with the positions b-1, b-2, and b-3 in Figure 6b.

Among the three grains found in Figure 6c, the middle grain shows a hexagonal array of dark dots, while the right- and left-side grains both exhibit undulated stripe patterns oriented along the O*y* direction. Despite the slight difference in the lattice orientation, the lattice planes of the three grains in part c are continuous across the grain boundaries and their spacing agrees with the Bragg spacing of (100) plane determined by the SAXS experiment.[2] That is, the (100) planes in the three grains are more or less parallel to the *xy* plane, which agrees with the major orientation, as illustrated in Figure 1a. The middle grain has $\phi \approx 90°$, and the left- and right-side grains have ϕ slightly different from 90°.

b. TEM Observations along the Oz Direction (Grain Boundaries between Grains Having Major Orientation). Figure 7 shows a "mosaic" (or the patch work) composed of 35 TEM images taken with the magnification large enough to recognize the microdomain structure and the grain boundaries for an ultrathin section cut parallel to *xy* plane. We did prepare the patch work by using a personal computer and reduced the size to fit the space of this paper. The black solid lines in the figure indicate the grain boundaries which can be easily seen in the original patch work. In the original patchwork corresponding to Figure 7, we can observe 11 grains of the hex-cyl divided by the black solid lines, all of which exhibit the striped patterns with the spacing identical to that of (110) plane estimated from the SAXS experiment[2] as will be partially clarified in Figure 8.

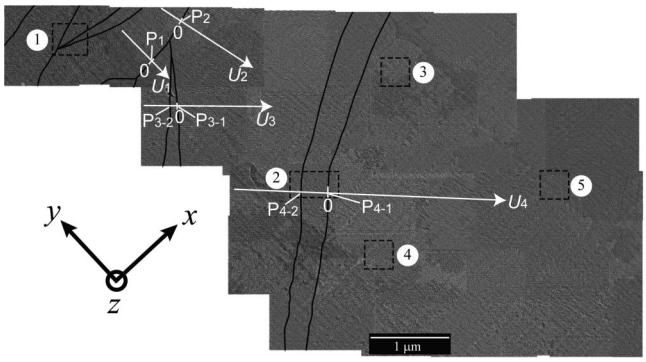

Figure 7. "Mosaic" image composed of 35 TEM images of the ultrathin section of the zone-heated SI bcp cut parallel to the *xy* plane and observed from the O*z* direction. Black solid lines indicate grain boundaries. The enlarged images of the areas encompassed by the broken rectangles designated by numbers 1−5 are shown in Figure 8. The white axes designated by U_i (i = 1−4), which perpendicularly cross the grain boundaries, indicate the paths, along which the change in the (110) lattice spacing was analyzed, the results of which will be shown in Figure 12.

It suggests that all of the grains observed in Figure 7 have the major orientation as illustrated in Figure 1a.

The area encompassed by the broken square designated by number 1 in Figure 7 contains four grains. The broken rectangle designated by number 2 contains a part of the slender grain that exists between the two large grains. The area encompassed by the broken squares designated by numbers 3, 4, and 5 belongs to the largest grain in Figure 7 which extends more than 5 μm^2 in the *xy* plane. Areas 1−5 were enlarged to the size with which the microdomains can be clearly observed and are shown in Figure 8a−e, respectively. It should be noted that the stripes in Figure 8 are less clear than those in Figure 4, partly because fewer cylinders are overlapped along (110) plane than along (100) plane in the ultrathin sections of the same thickness and partly because the spacing of (110) is smaller than that of (100) so that a slight misalignment of the orientation of (110) plane with respect to the direction normal to the ultrathin section causes the stripes less clear. In Figure 8a,b, black solid lines show the grain boundaries.

In Figure 8a, four grains have different orientation of hex-cyl from each other. Similarly, three grains in Figure 8b exhibit different orientation. That is, the orientation of the lattice plane of the hex-cyl changes from one grain to another, suggesting a different value of ϕ for each grain. This result is consistent with the model in Figure 1 in which the grains can take random values of ϕ from 0 to 180°. In Figure 8a,b, the dark stripes, corresponding to the PI cylinders in the (110) lattice planes, are continuous at the grain boundaries, which suggests the commensuration of the lattice plane at the grain boundaries, as will be discussed in section 4.2. In Figure 8c−e, the directions of the lattice planes are identical to one another, assuring that they are different parts of the same grain.

Grain boundaries between grains having major and minor orientations as observed along the O*z* direction were also identified from the (110) and (100) lattice planes. We found that these lattice planes do not commensurate at the grain boundaries of this class. The details are described in Figures S2 and S3 of Supporting Information 2.

4. Discussion

4.1. Relationship between ϕ and Interference Colors Observed by POM. In this section, we shall discuss the interference colors observed from the O*x* direction by POM (Figure 3a). The interference colors primarily depend on the form birefringence of a grain of hex-cyl and thickness of the specimens. The intrinsic form birefringence, Δn_f^0, of the cylinder is defined by

$$\Delta n_f^0 \equiv n_{||} - n_{\perp} \tag{1}$$

with[16]

$$n_{||}^2 = v_c n_c^2 + v_m n_m^2 \tag{2}$$

$$n_{\perp}^2 = n_m^2 \frac{(v_c + 1)n_c^2 + v_m n_m^2}{(v_c + 1)n_m^2 + v_m n_c^2} \tag{3}$$

where $n_{||}$ and $n_{\perp}$ are the refractive indices parallel and perpendicular to the cylinder axis, respectively, and n_c and n_m

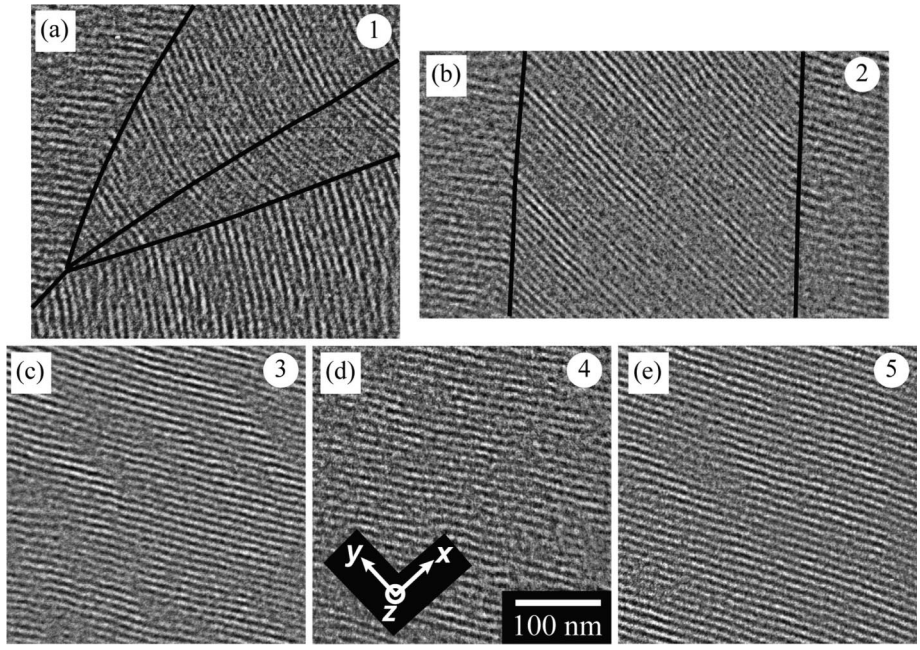

Figure 8. Parts a−e are enlarged TEM images of the areas encompassed by the broken rectangles designated by numbers 1−5 in Figure 7, respectively. Black solid lines show grain boundaries. The O*xyz* coordinate and the scale bar are common to parts a−e.

are the refractive indexes of the cylinder and the matrix, respectively. Although there are small orientational optical anisotropy,[17] due to the chains confined in the domain space, the small anisotropy may be negligible, except for the very strong segregation case. v_c and v_m are the volume fractions of the cylinder and the matrix, respectively ($v_c + v_m = 1$).

If the cylinder axes in a grain are oriented parallel to y axis or $\phi = 0°$ in Figure 1, its form birefringence observed from the Ox direction (defined as $\Delta n_{f,0}$) is equal to Δn_f^0. If $n_{||}$ and $n_\perp$ are very close, eq 1 can be approximated as follows:

$$n_{||}^2 - n_\perp^2 = (n_{//} + n_\perp)(n_{//} - n_\perp)$$
$$\cong 2n_{//}(n_{//} - n_\perp) = \frac{v_c v_m (n_c^2 - n_m^2)^2}{(v_c + 1)n_m^2 + v_m n_c^2} \quad (4)$$

Hence, Δn_f^0 is given by

$$\Delta n_f^0 \cong \frac{1}{2n_{||}} \frac{v_c v_m (n_c^2 - n_m^2)^2}{(v_c + 1)n_m^2 + v_m n_c^2} \quad (5)$$

We adopted the reference values of the corresponding homopolymers as n_c and n_m,[18,19] and v_c and v_m were estimated by using M_n of each block chain assuming that the densities of PS and PI microdomains to be equal to those of the corresponding homopolymers.[18−20] Thus, calculated value of $\Delta n_f^0 = 6.6 \times 10^{-4}$.

In the specimen, the cylinder axes in each grain are not always oriented parallel to y axis, so that the form birefringence of a grain of the hex-cyl, defined as $\Delta n_{f,\phi}$, changes depending on ϕ. Here we define refractive indices along the Oy direction and the Oz direction as n_y and n_z, respectively. If the hex-cyl in a grain has a rotational angle ϕ, the form birefringence of this grain for the observation along x axis is given by

$$\Delta n_{f,\phi} \equiv n_y - n_z = \Delta n_f^0 \cos^2 \phi \quad (6)$$

Here we note that the cylinder axis orients in the two-dimensional plane of Oxy.

In our actual observation, there are overlaps of the grains having different ϕ along the Ox direction, so that the observed interference colors reflect the averaged form birefringence, defined as $\Delta n_{f,x}$, along the Ox direction. Therefore, $\Delta n_{f,x}$ is described as follows:

$$\Delta n_{f,x} = \Delta n_f^0 \langle \cos^2 \phi \rangle \quad (7)$$

We evaluated $\Delta n_{f,x}$ from the interference color for each region shown in Figure 3f using eq 8:

$$\Delta n_{f,x} = \Gamma / d \quad (8)$$

where Γ and d are the observed retardation estimated from the interference color and the thickness of the specimen along the Ox direction, respectively. We then calculated $\langle \cos^2 \phi \rangle$ using eq 7. The results are given in Table 2. Here, in order to confirm that the observed interference colors are the first order ones, we inserted a retardation plate having $\Gamma_p = 530$ nm in such a way that the slow direction of the plate is perpendicular to the slow direction of the form birefringence of hex-cyl in the zone-heated specimen, so that the two retardations are compensated. The distinct colors such as bluish violet and red purple, which were observed before the insertion of the plate, became indistinct colors such as light and dark gray. Therefore, the interference colors observed without the plate are the first-order ones.

As already mentioned in section 3.1, the interference colors observed in Figure 3a can be classified into five different color levels (levels 1−5) (Table 2), although the specimen area was divided into 17 different regions as marked by the numbers in Figure 3f. According to eqs 7 and 8, each of the observed colors depends on $\langle \cos^2 \phi \rangle$ and reflects the superposition of the grains having different orientation of hex-cyl with respect to ϕ along the Ox direction. It should be noted that $\langle \cos^2 \phi \rangle = 1$, and 0, if the cylinder axes are oriented parallel to the Oy axis and Ox axis, respectively; $\langle \cos^2 \phi \rangle = {}^1/_2$ if ϕ is random. Thus, judging from the results shown in Table 2, the cylinder axes in region 6 in Figure 3 have a preferential orientation along the Oy axis, those in regions 5, 12, and 13 have almost random orientation, and those in regions 1, 3, 9, 10, 15, 17, and 8 have a preferential orientation along Ox axis. As shown in Figure 3f, each region having a single color does not exceed 0.35 mm along the Oy direction, but extends more than 0.95 mm along the Oz direction. The region having the largest length along the Oz direction is region 8, and the length is over 1.4 mm. Thus, each region has a columnar shape which extends macroscopically along the Oz direction. These columnar-shaped regions having a single color indicate that ϕ is constant along the Oz direction, although it varies along the direction perpendicular to the Oz direction. Therefore, the features shown in Figure 3f,h are consistent with the columnar grain model shown in Figure 1b.

4.2. Analysis of Grain Boundaries by TEM. In the characteristic orientation of hex-cyl formed in the zone-heated bcps, the cylinder axes of the hex-cyl are parallel to the xy plane, but its rotational angle around the z axis statistically varies randomly among different grains.[1,2] Huge grains were observed by POM as shown by Figure 3 and partially by TEM, and they are dominant in the zone-heated specimen. However, small grains were also observed in the periphery of the huge grains as revealed by the TEM images in Figure 7 and Figure S2 in Supporting Information 2. Now we focus on the morphology of the grain boundaries where two grains with different rotational angle of the hex-cyl are in contact. Are there any regularities in the grain boundary structures? TEM observation from the Oz direction may be most effective to clarify this point because the direction of cylinder axes can be observed directly in the xy plane.

Therefore, we analyzed the changes in the direction of cylinder axes at the grain boundaries by using the TEM images observed along the Oz direction. We focused on the grain boundaries between the grains having the major orientation because the weight fraction of which was 98−99%.[2] An example of the TEM images used for the analysis is shown in Figure 9. In order to characterize the grain boundaries, we measured the angles ω_1 and ω_2 between the grain boundary and (110) lattice plane of each grain defined by the direction of the stripes and the net angle θ_{12} between the (110) lattice planes of the two grains ($\theta_{12} = \omega_1 + \omega_2$). We also measured the spacings of stripes or (110) lattice planes in each grain, D_1 and D_2. An error of ±5° was involved in the measurement of the angles itself and an error of ±0.3 nm in the measurement of the spacing. The errors in ω_1, ω_2, and θ_{12} due to the inclination of the z axis with respect to the ultrathin sections are negligible. The errors in D_1 and D_2 due to inclination of the z axis are within 1.5%.

The inset at the top left of Figure 9 shows the enlarged image of the region encompassed by the square. The stripes or the lattice planes of the two grains are continuous at the grain boundary. The grain boundaries are very sharp; i.e., the orientation of the lattice planes within each grain is kept unchanged from a point far from the grain boundary to the point very close to the grain boundary. This smooth connectivity is the common feature in all grain boundaries observed between two grains having the major orientation. This implies that not only the lattice planes but also the cylinders themselves are continuous at the grain boundaries, when we take the results of

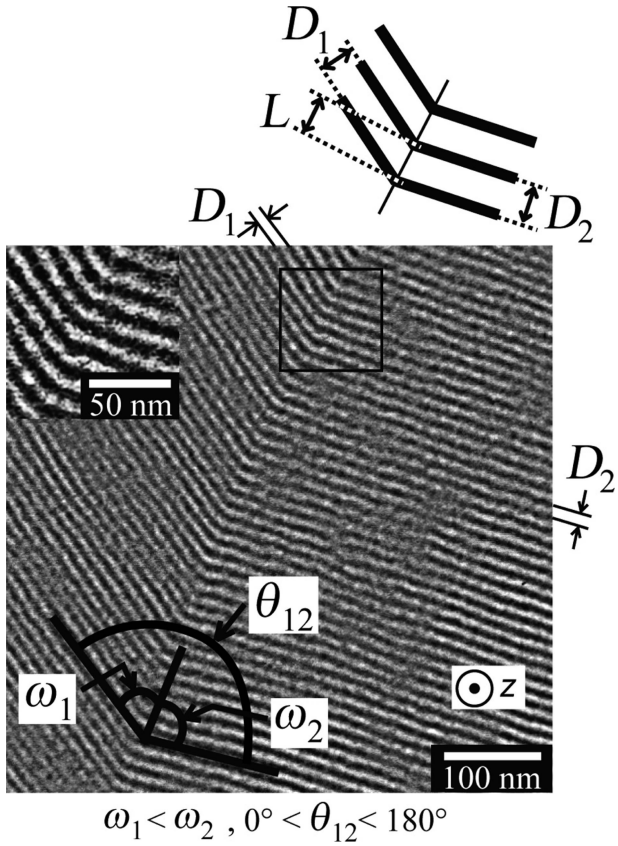

Figure 9. Definition of the parameters ω_1, ω_2, θ_{12}, D_1, D_2, and L for the grain boundary analysis of the TEM images observed from the Oz direction. The angles between the grain boundary and the (110) lattice planes of the two grains are designated as ω_1 and ω_2, and the angle between the lattice planes of the two grains is designated as θ_{12}. ω_2 is defined as the angles having a larger angle between the two angles ω_1 and ω_2. The (110) lattice spacings of the two grains are designated as D_1 and D_2, and the periodic distance of the lattice spacing along the grain boundary is defined as L.

Jinnai et al.[5] into account. This feature imposes the following relation among the values of ω_1, ω_2, D_1, D_2, and L:

$$L = \frac{D_1}{\sin \omega_1} = \frac{D_2}{\sin \omega_2} \tag{9}$$

where L is the periodicity of the lattice planes along the grain boundaries. When the domain structure in each grain reaches the "quasi"-thermal equilibrium state, D_1 and D_2 should satisfy

$$D_1 = D_2 \equiv D_e \tag{10}$$

where D_e is the equilibrium spacing. The term "quasi" was added because the grain boundary is always accompanied an excess free energy relative to ordered domains in the bulk.[21] Thus, the following relations are deduced from eqs 9 and 10:

$$\omega_1 = \omega_2 \equiv \omega_e \tag{11}$$

$$\theta_{12} = 2\omega_e \tag{12}$$

where ω_e is the angle between the grain boundary and each lattice plane in the quasi-equilibrium state. Equation 11 is schematically visualized in Figure 10a.

On the other hand, there is a case where two sets of lattice planes cannot be continuous at the grain boundary, even if two grains can satisfy eq 11; e.g., there is a case where the lattice planes in the two grains are parallel, but their positions are

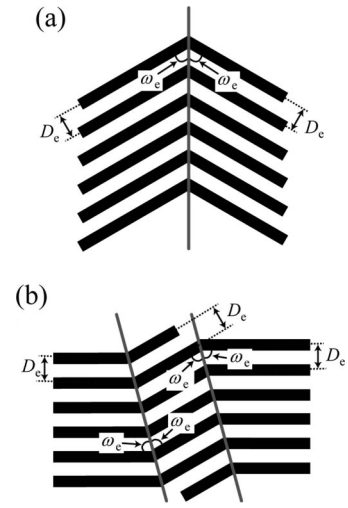

Figure 10. (a) Schematic illustration of the grain boundary in the quasi-equilibrium state satisfying eq 11. (b) A middle grain "connecting" the two staggered grains on the left- and right-hand side in the quasi-equilibrium state.

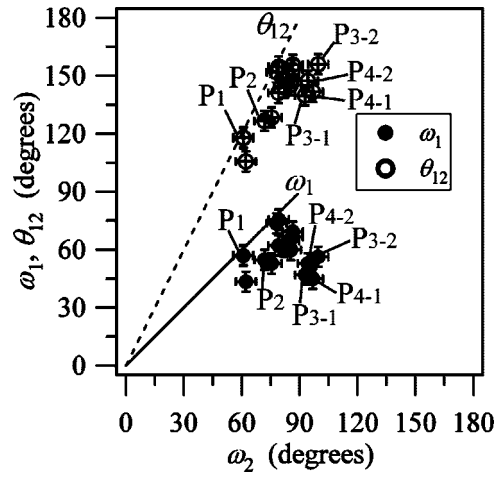

Figure 11. Results of the grain boundary analysis of the TEM images observed from Oz direction. The measured values of ω_1 and θ_{12} are plotted as a function of ω_2. The data marked by P_1, P_2, P_{3-1}, P_{3-2}, P_{4-1}, and P_{4-2} denote the data taken at points on the grain boundaries designated in Figure 7. The solid and dashed lines indicate the predicted lines from eqs 11 and 12, respectively.

staggerd along the direction perpendicular to the planes, as shown in Figure 10b. In this case, an interstitial grain having different orientation from the orientation of the two grains is formed, and lattice planes become continuous through interstial grains. Here, eq 11 is satisfied at each of the two grain boundaries, as shown in Figure 10b.

ω_1 and θ_{12} are plotted as functions of ω_2 in Figure 11. The solid and dashed lines in Figure 11 indicate eqs 11 and 12, respectively. In order to simplify the plot showing a relationship between ω_1 and ω_2, we define the angle ω_2 as the angle having a larger angle between the two angles ω_1 and ω_2. Both plots show the trends qualitatively similar to eqs 11 and 12. However, the experimental data quantitatively deviate from those in the quasi-equilibrium state. The deviation of the data points from eq 11 suggests $\omega_1 \neq \omega_2$, and hence $D_1 \neq D_2$, because eq 9 should be satisfied even when the deviation is large as long as the commensuration of the lattice planes occurs.

In order to investigate the mismatch between the spacings D_1 and D_2, we measured the spacing as a function of the distance U_i from the grain boundaries along the direction perpendicular

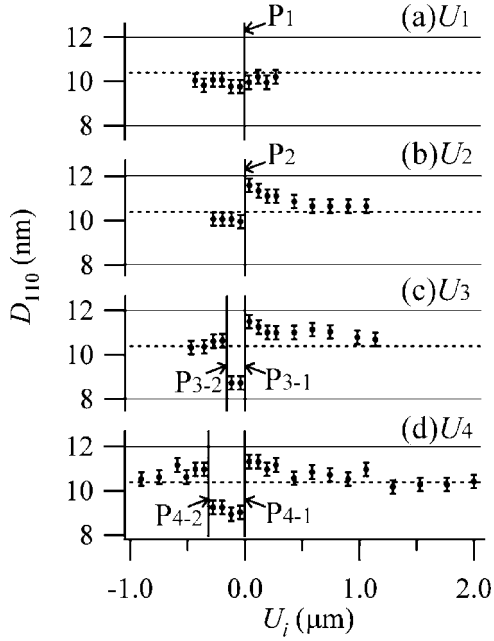

Figure 12. Change in (110) spacing (D_{110}) along the direction perpendicular to the grain boundary is plotted against the distance U_i from the grain boundary for four different cases as designated by axes U_1, U_2, U_3, and U_4 in Figure 7. The vertical solid lines indicate the positions of the grain boundaries, and P_1, P_2, P_{3-1}, P_{3-2}, P_{4-1}, and P_{4-2} correspond to those in Figures 7 and 11. Horizontal dotted lines indicate the (110) spacing obtained by the SAXS experiment.

to the boundary for each data point in Figure 11, where annotations P_1, P_2, P_{3-1}, P_{3-2}, P_{4-1}, and P_{4-2} correspond to the positions in the grain boundaries designated in Figure 7. The spacing of (110) planes, D_{110}, measured along U_1, U_2, U_3, and U_4 axes designated in Figure 7 are plotted against the distance U_i ($i = 1$, 2, 3, and 4) in Figure 12a−d, respectively. In Figure 12, the vertical solid lines indicate the positions of the grain boundaries, and the horizontal dotted lines indicate the average spacing obtained from the SAXS experiment.[2]

The axis U_1 crosses the grain boundary at P_1 as shown in Figure 7, and there are almost no changes in the spacing across P_1 as shown in Figure 12a. In this case, the lattice spacings near the grain boundary seem to have the values close to the equilibrium value at P_1, and the data point of P_1 in Figure 11 is close to the calculated data based on the quasi-equilibrium state. The axis U_2 crosses the grain boundary at P_2, and the spacing changes abruptly at P_2. In the grain of $U_2 > 0$, D_{110} increases with decreasing U_2. This result indicates that the lattice spacing is in a nonequilibrium state at P_2, especially in the grain of $U_2 > 0$, so that the data of ω_1 at P_2 in Figure 11 differs from the calculated data. The axes U_3 and U_4 cross a set of grain boundaries at P_{3-1} and P_{3-2} and P_{4-1} and P_{4-2}, respectively. The data points of these grain boundaries show the largest deviation from the calculated data based on eq 11 as shown in Figure 11, and as shown in Figure 12c,d, the narrow grains sandwiched by the two large grains have much smaller spacing than that of the two neighboring grains. This is the reason why the deviation of the data points for these cases from the predicted quasi-equilibrium values is the largest in Figure 11. These results indicate that the microdomains can have the nonequilibrium lattice spacing in the vicinity of the grain boundaries in order to bring about the commensuration of the lattice planes at the grain boundaries. Indeed, when the measured D_{110}s were used as D_1 and D_2, the measured ω_1s and ω_2s satisfy eq 9.

The pieces of information concerning the GBS and the nonequilibrium lattice spacings gave us some hints to speculate a possible process which brought about formation of such a chratacteristic "columnar" grain structure as observed by POM and TEM: (i) The disordered SI bcp melt must have started to order through the nucleation and growth of the hex-cyl simultaneously at different points on the glass surface when it reached T_{ODT}. (ii) Subsequently, the resulting nuclei should be able to laterally grow in the xy plane perpendicular to the ∇T axis by consuming supercooled disordered melt without any restrictions,[22] while new nuclei could appear at other points on the glass surface. (iii) The new nuclei could also laterally grow in the plane parallel to the glass surface, but their growth should be restricted by the grains which have already grown to occupy the large area on the plane. (iv) Finally, impingements occur between the grains. (v) The successive sequential ordering in the direction parallel to the ∇T axis should occur naturally just by following the movement of ∇T, resulting in formation of the "columnar" grains.

Process (ii) mentioned above should result in the large grains having more or less elliptical shapes on statistical average as shown in Figure 3h because of the growth without any restrictions, while process (iii) should result in the small grains having the cross-sectional shapes far from the elliptical shapes as shown in Figure 7 and Figure S2 in Supporting Information 2. The impingement in process (iv) could induce commensuration of the lattice planes between the adjacent grains having the major orientation with a free energy cost of having the nonequilibrium lattice spacing. However, it could not induce commensuration between the grain having major orientation and the grain having minor orientation as demonstrated in Figure S3 in Supporting Information 2 because the free energy cost of deformation required to match the two different lattice spacings is too large. Although the origin of the commensuration with a cost of having the nonequilibrium lattice spacing is not yet clarified at this moment, we plan to investigate this problem further by TEM tomography technique in the near future.

5. Concluding Remarks

We have previously investigated the "columnar" texture of cylinder-forming bcp produced by the zone heating process with the SAXS analyses.[1−3] The real-space analyses of the texture with POM and TEM observations in this study directly verified the "columnar" shape of the grains and with the special orientation of the hex-cyl. The POM images also indicate that the cross sections of the "columnar" grains have more or less elliptical shapes on statistical average and extend over 60−130 μm in the plane parallel to xy plane. The extension of the columnar grain along the ∇T direction (the Oz direction) was found to be huge, as large as 1.4 mm.

Focusing on the grain boundaries, we found that the lattice planes are continuous at the grain boundary for any two grains with the major orientation (commensurated grain boundary), but incommensurate grain boundaries were observed between the two grains: one with the major orientation and the other with the minor orientation. Moreover, in the case of the commensurated grain boundary, the angles ω_1 and ω_2 between the grain boundary and the spacings D_1 and D_2 of (110) lattice planes are kept to satisfy the condition that the periodic distance L of the lattice plane along the grain boundary in one grain matches with that in the other grain (eq 9). In order to achieve this condition, the spacings D_1 and D_2 near the grain boundary happened to be modified to result in a nonequilibrium value for some cases.

Acknowledgment. We thank S. Akasaka (Kyoto University) for his technical assistance for TEM and POM observations. This work was supported in part by a Grant-in-Aid for Scientific Research (under Grant 17005004(S)) from Japan Society for the Promotion of Science (JSPS).

Supporting Information Available: Supporting Information 1, containing text that discusses a small columnar grain observed with the incident electron beam along the O*x* direction as well as Figure S1, the mosaic image composed of seven TEM images observed from the O*x* direction; and Supporting Information 2, containing text that discusses grain boundaries between grains having major and minor orientations as observed with incident electron beam along the O*z* direction as well as Figure S2, a mosaic image composed of 19 TEM images of the ultrathin section of the zone-heated SI bcp cut parallel to the *xy* plane and observed from the O*x* direction, and Figure S3, TEM images of the special areas in Figure S2. This material is available free of charge via the Internet at http://pubs.acs.org.

References and Notes

(1) Mita, K.; Tanaka, H.; Saijo, K.; Takenaka, M.; Hashimoto, T. *Macromolecules* **2007**, *40*, 5923.
(2) Mita, K.; Tanaka, H.; Saijo, K.; Takenaka, M.; Hashimoto, T. *Macromolecules*. **2008**, *41*, 6780.
(3) Mita, K.; Tanaka, H.; Saijo, K.; Takenaka, M.; Hashimoto, T. *Macromolecules*. **2008**, *41*, 6787.
(4) The effect of the Kapton film surfaces (which contact with the specimen surfaces normal to the *y* axis) as well as the PTFE surfaces (which contact with the specimen surfaces normal to the *x* axis) on orientation of hex−cyl were found to be negligible. This was well described in the second paragraph of section 3.3 (page 5927) of ref 1, though "PET sheets" normal to the *y* axis in the paragraph of ref 1 was indicated to be a mistake and should be "Kapton sheets" as corrected in ref 3, and also the "PET sheets" normal to the *x* axis in the paragraph of ref 1 was a mistake and should be "PTFE surfaces".
(5) Jinnai, H.; Yasuda, K.; Nishi, T. *Macromol. Symp.* **2006**, *245*, 170.
(6) Park, C.; Yoon, J.; Thomas, E. L. *Polymer* **2003**, *44*, 6725.
(7) Kléman, M. *Points, Lines, and Walls*; John Wiley and Sons: New York, 1983.
(8) Gido, S. P.; Gunther, J.; Thomas, E. L.; Hoffman, D. *Macromolecules* **1993**, *26*, 4506.
(9) Gido, S. P.; Thomas, E. L. *Macromolecules* **1994**, *27*, 849.
(10) Gido, S. P.; Thomas, E. L. *Macromolecules* **1994**, *27*, 6137.
(11) Gido, S. P.; Thomas, E. L. *Macromolecules* **1997**, *30*, 3739.
(12) Nishikawa, Y.; Kawada, H.; Hasegawa, H.; Hashimoto, T. *Acta Polym.* **1993**, *44*, 192.
(13) Bodycomb, J.; Funaki, Y.; Kimishima, K.; Hashimoto, T. *Macromolecules* **1999**, *32*, 2075.
(14) Philipse, A. P.; Vrij, A. *J. Colloid Interface Sci.* **1989**, *128*, 121.
(15) Rochow, T. G.; Tucker, P. A. *Introduction to Microscopy by Means of Light, Electrons, X Rays, or Acoustics*; Plenum Press: New York, 1994.
(16) Wiener, O. *Abh. Math-Phys. Kl. Saechs. Ges. Wiss.* **1912**, *32*, 507.
(17) Hashimoto, T.; Shibayama, M.; Kawai, H.; Meier, D. J. *Macromolecules* **1985**, *18*, 1855.
(18) Schrader, D. In *Polymer Handbook*, 4th ed.; Brandrup, J., Immergut, E. H., Grulke, E. A., Eds.; John Wiley & Sons Inc.: New York, 1999; p V-91.
(19) Furuta, I.; Kimura, S.; Iwama, M. In *Polymer Handbook*, 4th ed.; Brandrup, J., Immergut, E. H., Grulke, E. A., Eds.; John Wiley & Sons Inc.: New York, 1999; p V-5.
(20) υ_c and υ_m are calculated by following equation: $\upsilon_i = V_i/(V_c + V_m)$ and $V_i = M_{n,i}/\rho_i$, where i indicates c or m, $M_{n,i}$ is the number-average molecular weight of the block chains comprising the cylinders or the matrix, and ρ_i is the density of homopolymer[18,19] corresponding to the block chains comprising the cylinders or the matrix. $M_{n,i}$ was determined by gel permeation chromatography (GPC).
(21) Hashimoto, T.; Koizumi, S.; Hasegawa, H. *Macromolecules* **1994**, *27*, 1562.
(22) The hex−cyl grains may have anisotropic growth rate, slower along the cylinder axis than the direction normal to it.[23,24] In such a case, grain should have an oblate ellipsoidal shape having the axis of revolution parallel to the cylinder axis, so the cross section normal to the ∇T axis should be ellipsoidal.
(23) Koizumi, S.; Hasegawa, H.; Hashimoto, T. *Macromolecules* **1994**, *27*, 6532.
(24) Sakamoto, N.; Hashimoto, T. *Macromolecules* **1998**, *31*, 8493.

MA801750C